 CMES, vol.116, no.3, pp.323-347, 2018

Improved State-Based Peridynamic Lattice Model Including Elasticity, Plasticity and Damage

Siavash Nikravesh[1, *] and Walter Gerstle[1]

Abstract: In this study, a recently developed peridynamic lattice model called the "State-based Peridynamic Lattice Model" (SPLM) is improved and demonstrated. In the SPLM, rather than as a continuum, solids are simulated using a close-packed lattice of peridynamically interacting particles. The new SPLM approach advances the SPLM model by improving the damage and plasticity models. Elasticity, plasticity and damage are coupled in this approach. A robust method for damage initiation is developed. A new damage model called the "two-spring damage model" allows damage to localize to a single lattice particle, thus allowing highly localized damage (cracks) to emerge in a realistic manner. A plasticity model that includes hardening, softening, and damage due to plasticity is proposed and demonstrated. Peridynamic boundary effects are modeled efficiently and reasonably. The improved SPLM method is then employed to simulate three common concrete laboratory tests: Uniaxial tension, uniaxial compression, and the Brazilian split cylinder test. The SPLM results are then compared with results from the earlier SPLM model, with simplified classical predictions, and with laboratory results. By solving the same benchmark problems using various lattice rotations and lattice spacings, the approach is demonstrated to be sufficiently objective to be a useful engineering tool to predict the essentially random behavior of concrete laboratory specimens. The improved SPLM demonstrates significant improvements over the previously published version and is found to simulate concrete structures accurately and efficiently using far less computational effort than comparable computational simulation methods.

Keywords: Peridynamics, SPLM, lattice, damage, plasticity, fracture, concrete.

1 Introduction

In 2000, an alternative approach to classical continuum mechanics, introduced by Silling [Silling (2000)], called the "peridynamic" model was proposed. The peridynamic model uses nonlocal interparticle force interactions and thus avoids an assumption of differentiability of the displacement field. In this theory, a nonlocal pairwise peridynamic force function, which is a function of reference and deformed particle positions, is assumed. In the initial approach [Silling (2000)], later called the "bond-based peridynamic model", the pairwise force function between two interacting particles was assumed to be a function

[1] Department of Civil, Construction and Environmental Engineering, University of New Mexico, Albuquerque, NM, USA.

[*] Corresponding Author: Siavash Nikravesh. Email: siavashnk@unm.edu.

only of the relative positions between the interacting pair of particles. The bond-based model was found to be insufficiently general, forcing a specific Poisson's ratio, and lacking the capability to adequately model isochoric plastic deformations. In Gerstle et al. [Gerstle, Sau and Silling (2007)], these shortcomings were partially resolved by the development of the "micropolar bond-based peridynamic model" which includes rotational degrees of freedom. Also, in 2007, a second continuum peridynamics approach, called the "state-based peridynamic model", was published [Silling, Epton, Weckner et al. (2007)]. In the state-based approach, the pairwise peridynamic force function is not only a function of the positions of the two adjacent interacting particles, but is also a function of other neighboring particles within a local neighborhood. The state-based model allowed for entirely general solid models, without the limitations of the bond-based methods. However, compared to the bond-based methods, the state-based approach is more complex. In addition, due to requiring many more particles in the computation of the pairwise force function, the computational cost of the state based approach is much higher than that of the bond-based model. Some recent and useful studies of continuum peridynamics are found in Silling et al. [Silling and Askari (2005); Macek and Silling (2007); Silling and Lehoucq (2010); Mitchell, Silling and Littlewood (2015); Silling, Littlewood and Seleson (2015); Seleson and Littlewood (2016); Rabczuk and Ren (2017); Silling (2017); Silling, Parks, Kamm et al. (2017); Foster and Xu (2018); Hattori, Trevelyan and Coombs (2018); Pasetto, Leng, Chen et al. (2018)].

In both the bond-based and the state-based peridynamic approaches, the reference material space is treated as a continuum. Hence, Silling's methods are continuum peridynamic models. In 2015, Gerstle [Gerstle (2015)] presented state-based peridynamics using a lattice. The proposed method is called the "State-Based Peridynamic Lattice Model" (SPLM). In the SPLM, the material reference domain is represented by a finite number of particles in a regular lattice configuration. With the SPLM, the topological neighborhood of each particle is assumed to remain invariant throughout the simulation. The peridynamic force functions in the SPLM are explicitly designed to minimize the required number of neighbors within the material horizon of each particle. Thus, the SPLM, while not perfectly objective, is much more efficient, in terms of computational effort, than the continuum peridynamic approach. Further studies showed that the initial published version [Gerstle (2015)] of the SPLM was insufficiently objective: the simulations including damage and plasticity did not accurately match classical solutions, did not accurately replicate experimental behavior, did not converge well with lattice refinement, and were somewhat sensitive to lattice rotation, translation, and particle spacing.

In this study, improved SPLM peridynamic force functions are developed and demonstrated. In the new model, a single damage variable is associated with the particle instead of with the bonds; thus, we call this damage model a particle-based isotropic damage model. The new "two-spring" damage model has the capability of modelling more localized stretch states and consequent damage than in the previous SPLM model. The two-spring damage model allows adjacent particles with greatly differing damage and stretch states to interact in a reasonable way. A suitable hardening and softening plasticity model, including damage caused by excessive plastic work, is also proposed. An improved SPLM explicit dynamic solution algorithm is also presented.

The improved SPLM is then demonstrated, using plain stress simulations of three common concrete laboratory tests. The results are compared with those of classical approaches and with the behavior of laboratory tests. The approximate objectivity of the approach is demonstrated by simulating each test with varying SPLM lattice rotations.

The SPLM simulation results demonstrate sufficient realism and superior computational efficiency in modelling concrete structures. While we recognize that the SPLM is not absolutely objective in the sense of tensor mathematics and continuum mechanics, the SPLM approach "exploits an engineer's tolerance for imprecision" (to paraphrase a quote by Zadeh [Zadeh (1973)], is reasonably objective, is physically realistic, and is more computationally efficient than other computational models presented in the literature of which we are aware. Once correctly calibrated, the SPLM recognizes the meso-mechanical size scale of the material being modeled and requires no tedious (and ultimately unhelpful) convergence studies.

2 Improved State-based Peridynamic Lattice Model (SPLM)

In this section, the main differences between the continuum and discrete peridynamic formulations are demonstrated, and a revised formulation of the SPLM is proposed and discussed.

Continuum state-based peridynamic theory was initially proposed by Silling et al. [Silling, Epton, Weckner et al. (2007)] as an alternative to classical continuum mechanics methods. Roughly following reference [Silling, Epton, Weckner et al. (2007)], the peridynamic equation of motion of particle $\boldsymbol{X}$ is expressed as

$$\rho(\boldsymbol{X})\ddot{\boldsymbol{x}}(\boldsymbol{X},t) = \int_{H_{\boldsymbol{x}}} \boldsymbol{f}_{\boldsymbol{X}\boldsymbol{X}'}\, dV_{\boldsymbol{X}'} + \boldsymbol{B}(\boldsymbol{X},t), \tag{1}$$

where $\boldsymbol{X}$ and $\boldsymbol{X}'$ are the initial, reference position vectors of two neighboring particles within the peridynamic horizon $H_{\boldsymbol{X}}$ of particle $\boldsymbol{X}$, $\rho(\boldsymbol{X})$ is the mass density associated with particle $\boldsymbol{X}$ in the reference configuration, $\boldsymbol{x}$ is the deformed position vector of particle $\boldsymbol{X}$, $\boldsymbol{B}$ is the externally applied body force vector, t is time, and $\boldsymbol{f}_{\boldsymbol{X}\boldsymbol{X}'}$ is a function called the "pairwise force function", described in terms of force states as

$$\boldsymbol{f}_{\boldsymbol{x}\boldsymbol{x}'} = \underline{\boldsymbol{T}}[\boldsymbol{X},t]\langle\boldsymbol{X}'-\boldsymbol{X}\rangle - \underline{\boldsymbol{T}}[\boldsymbol{X}',t]\langle\boldsymbol{X}-\boldsymbol{X}'\rangle. \tag{2}$$

Here, $\underline{\boldsymbol{T}}$ is a "force state", which is a vector function of the deformation of all the bonds connected to particle $\boldsymbol{X}$ in the neighborhood $H_{\boldsymbol{X}}$ of particle $\boldsymbol{X}$. The mathematical notation $\underline{\boldsymbol{T}}[\boldsymbol{X},t]\langle\boldsymbol{X}'-\boldsymbol{X}\rangle$ means that the force state, $\underline{\boldsymbol{T}}$, is acting on particle $\boldsymbol{X}$, at time t, and on the reference bond $\langle\boldsymbol{X}'-\boldsymbol{X}\rangle$. In this paper, following Gerstle [Gerstle (2015)], we employ a revised definition of the force state $\underline{\boldsymbol{T}}$ that is more suitable for a lattice reference configuration. We also propose a revised definition of the pairwise force function, $\boldsymbol{f}_{\boldsymbol{x}\boldsymbol{x}'}$, that is more general than what is employed by Silling (Eq. (2)) and more proper when incorporating localized damage and plasticity.

The constitutive peridynamic equation of motion (Eq. (1)) is based upon the following assumptions:

(1) Particle $\boldsymbol{X}$ moves in accordance with Newton's second law.
(2) The topology of the particles surrounding particle $\boldsymbol{X}$ does not change during the motion.

(3) The peridynamic family of particle $\boldsymbol{X}$ is a continuum. In other words, the reference material domain is assumed to be a continuum.
(4) The pairwise force function ($\boldsymbol{f}$), or essentially force state ($\underline{\boldsymbol{T}}$), is Reimann integrable, and the integral in Eq. (1) converges uniformly [Silling, Epton, Weckner et al. (2007)].

The state-based peridynamic approach, proposed by Silling et al. [Silling, Epton, Weckner et al. (2007)], is a more general formulation than classical continuum mechanics because, by employing an appropriate peridynamic constitutive model, it can simulate both continuous and discontinuous deformation fields. Silling presented state-based peridynamics as an alternative continuum approach because it is developed based upon a continuum reference domain. However, the state-based continuum peridynamic model must be discretized to be of practical use. Usually discretized using a particle lattice, the continuum model requires very many lattice particles be included in the family of each particle. In addition, as cracks evolve, very many peridynamic bonds spanning the crack trajectory must be fully broken to represent a discrete crack.

Classically, structural models have been defined using crisp analytical surface boundaries. This is a mathematical convenience that may not accurately represent realistic boundaries of solids. With peridynamics, representation of these artificially crisp boundaries is a modelling burden that is neither helpful nor necessary. Indeed, particles in the structure that are closer than the material mesoscale to an (artificially assumed) analytical boundary cannot be considered to consist of the same material as the part of the structure that is far (compared to the mesoscale) from the boundary. Classical solid mechanics assumes that the representative volume element is infinitesimal, but this is a reasonable assumption neither for solids with mesoscale not much smaller than the macroscale, nor for solids that crack. We dispense completely with the explicit concept of "analytical boundary" when using a particle lattice to model a structure. Boundaries emerge naturally because lattice particles are missing neighbors initially, as well as because during the simulation lattice particles may become connected to fully damaged bonds. Thus, as damage develops within a lattice body, new boundaries may emerge naturally. Emergence of boundaries is much more difficult with classical continuum representations.

In this study, a lattice-based material space for the state-based peridynamic theory is employed. Consider a spherical (circular in 2D) peridynamic family H_i, centered upon lattice particle *i*, with radius (material horizon) δ. Depending upon the material horizon δ, the "family" of particle *i* includes a finite number, N_{P_i}, of particles interacting with *i*. An ordered list of lattice particles is called the "neighbor-list of particle *i*" (this list does not include particle *i*). It is assumed that particles not in the family of particle *i* will not have any force interaction with particle *i*. In the SPLM approach it is assumed that particle *i* interacts with each particle within its family via a bond. The acceleration of particle *i* at time step *n*, $\ddot{\boldsymbol{x}}_i^n = \ddot{\boldsymbol{x}}(\boldsymbol{X}_i, t^n)$, is calculated as

$$m_i \ddot{\boldsymbol{x}}_i^n = \sum_{j=1}^{N_{P_i}} (\boldsymbol{F_b})_{ij}^n + \boldsymbol{B}_i^n. \tag{3}$$

Eq. (3) is the SPLM discrete equation of motion. In Eq. (3), m_i is the mass of particle i, N_{P_i} is the total number of particles within the family of particle i, $\boldsymbol{B}_i^n$ is the body force acting on particle i at time step n, and $(\boldsymbol{F_b})_{ij}^n$ is the bond force acting on particle i in the direction of deformed bond ij, and at time step n.

In the improved SPLM, in the time-discretized explicit dynamic approach, the bond force between particles i and j, $(\boldsymbol{F_b})_{ij}^n$, at time step n is assumed to be a function $\boldsymbol{\Phi}$ of force states $(\boldsymbol{F_s})_{ij}^{n-1}$ and $(\boldsymbol{F_s})_{ji}^{n-1}$ computed at time step $n-1$:

$$(\boldsymbol{F_b})_{ij}^n = \boldsymbol{\Phi}\big((\boldsymbol{F_s})_{ij}^{n-1}, (\boldsymbol{F_s})_{ji}^{n-1}\big). \tag{4}$$

By computing the bond forces from the force states calculated in the previous time step (rather than in the current time step), we ensure that the computed bond forces are independent of the order in which the particles are visited within a given time step. Because with an explicit time integration approach the time steps must be very small to satisfy the dynamic stability criterion, this approximation is found to be acceptable, as particle positions and state variables vary little from one time step to the next. Also, if a state variable does jump from one time step to the next, it makes little difference in precisely which time step the jump occurs, as the time steps are so small. No iterations are performed within a given time step; we use a strictly Eulerian time integration approach.

The definition of the force state $(\boldsymbol{F_s})_{ij}^n$ in SPLM is discussed in Section 2.1. The function $\boldsymbol{\Phi}$ in the SPLM satisfies the following conditions. Firstly, Newton's third law is satisfied so that $(\boldsymbol{F_b})_{ij}^n = -(\boldsymbol{F_b})_{ji}^n$. Secondly, the bond forces $(\boldsymbol{F_b})_{ij}^n$ are assumed to be collinear with the deformed particle positions. Finally, the force state, $(\boldsymbol{F_s})_{ij}^n$, is not a function only of the attributes of particles i and j, but also of the attributes of all of the lattice particles within in the family of particle i.

2.1 Linear-elastic SPLM

The hexagonal lattice (in 2D), and the face-centered cubic lattice (in 3D) are chosen because of their high degree of symmetry [Gerstle (2015)]. In this paper, for simplicity, and without loss of generality, we consider only the 2D case. With the 2D hexagonal lattice, as shown in Fig. 1, the simplest neighbor list of particle i possesses six potential neighbors. Except for missing lattice neighbors on the boundary, the number of neighbors for each interior particle is $Np_i = 6$. The radius of the horizon of every particle is fixed as the lattice spacing, L_0. The finite volume associated with each particle is $\Delta V_i = \Delta V = (\sqrt{3}/2)t{L_0}^2$, shown in Fig. 1a, where t is the thickness of the 2D body.

The bond force between two particles takes on the minimum of the absolute value of the two force states evaluated with respect to the two connected particles, with due respect to sign, except that if the signs of the two force states are different, the average of the two force states is used. This modification to the original state-based theory [Silling, Epton, Weckner et al. (2007); Gerstle (2015)] is advantageous if the difference in damage, and hence force states, between adjacent lattice particles is large.

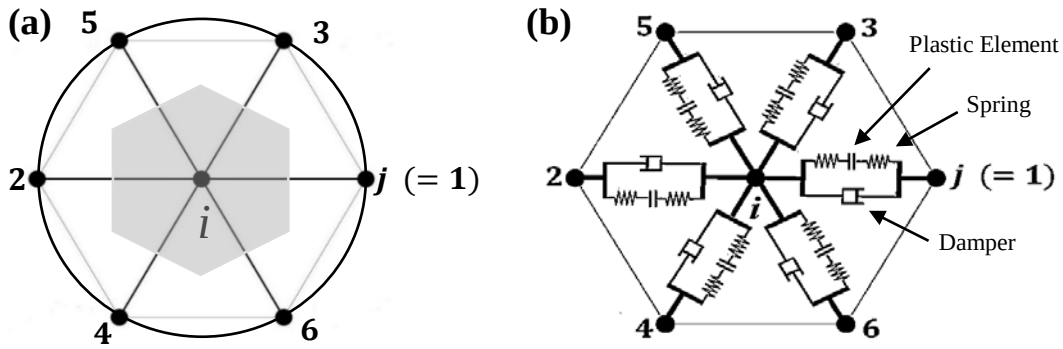

Figure 1: General re-formulated SPLM model. (a) Lattice topology and bond numbering order. The associated volume of the particle *i* (= $\Delta \boldsymbol{V}$) is shown in gray. (b) SPLM elasto-plastic damage model including two serial springs, a plastic element, and an internal damper within each bond

Regarding the lattice topology, the bonds are numbered from 1 to 6 in the order shown in Fig. 1, thus simplifying the computations. Opposing bonds are called complementary bonds. Thus, Bonds 1 and 2 are complementary, etc.

The bond forces $(\boldsymbol{F_b})_{ij}^{n}$ are calculated from bond states $(\boldsymbol{F_s})_{ij}^{n-1}$ in Eq. (4) as

$$(\boldsymbol{F_b})_{ij}^{n} = \boldsymbol{\Phi}\left((\boldsymbol{F_s})_{ij}^{n-1}, (\boldsymbol{F_s})_{ji}^{n-1}\right) = \begin{cases} min\left\{\left|(F_s)_{ij}^{n-1}\right|, \left|(F_s)_{ji}^{n-1}\right|\right\} \times sign((F_s)_{ij}^{n-1}) & if \quad (F_s)_{ij}^{n-1} \times (F_s)_{ji}^{n-1} > 0 \\ \frac{1}{2}\left((F_s)_{ij}^{n-1} + (F_s)_{ji}^{n-1}\right) & if \quad (F_s)_{ij}^{n-1} \times (F_s)_{ji}^{n-1} \leq 0 \end{cases} \tag{5}$$

In the original linear-elastic SPLM [Gerstle (2015)], the force state $(\boldsymbol{F_s})_{ij}$ acting on particle *i* in direction of particle *j*, is assumed as a linear combination of the elastic stretch $(S_e)_{ij}$ between *i* and *j*, as well as of the summation of the stretches of all the other bonds in the horizon of particle *i*. Hence, $(F_s)_{ij}$ is defined as

$$(F_s)_{ij} = a(S_e)_{ij} + b\sum_{m=1}^{6}(S_e)_{im}, \tag{6}$$

where the peridynamic elastic constants a and b are associated with particle *i*, and $(S_e)_{ij}$ is the elastic stretch in bond *ij*, defined as

$$(S_e)_{ij} = (S_T)_{ij} - \frac{1}{2}\left((S_P)_{ij} + (S_P)_{ji}\right), \tag{7}$$

where $(S_T)_{ij}$ and $(S_P)_{ij}$ are, respectively, the total stretch and the plastic stretch between particles *i* and *j*. Note that for the linear elastic case, the plastic terms in Eq. (7) are null. The total stretch, $(S_T)_{ij}$, is defined based on the current length, L, and reference length, L_0, of the bond between particles *i* and *j*, as

$$(S_T)_{ij} = \left(\frac{L-L_0}{L_0}\right)_{ij}, \tag{8}$$

where $L = \sqrt{(x_j - x_i)^2 + (y_j - y_i)^2}$ and $L_0 = \sqrt{(X_j - X_i)^2 + (Y_j - Y_i)^2}$, and where (x, y) and (X,Y) are, respectively, the coordinates of the particles in the current and the reference configurations. The force-stretch relation is expressed in matrix form as

$$\boldsymbol{F}_{\boldsymbol{S}_i} = \boldsymbol{K}_i \boldsymbol{S}_{\boldsymbol{e}_i}, \tag{9}$$

where

$$\boldsymbol{F}_{\boldsymbol{S}_i} = \left[(F_s)_{ij}\right]_{6\times 1} = \left\{(F_s)_{i1}, \dots, (F_s)_{ij}, \dots, (F_s)_{i6}\right\},$$

$$\boldsymbol{S}_{\boldsymbol{e}_i} = \left[(S_e)_{ij}\right]_{6\times 1} = \left\{(S_e)_{i1}, \dots, (S_e)_{ij}, \dots, (S_e)_{i6}\right\},$$

and the micro-elastic stiffness matrix associated with particle *i*, $\boldsymbol{K}_i$, is

$$\boldsymbol{K}_i = \boldsymbol{K} = \begin{bmatrix} a+b & b & \cdots & b & b \\ b & a+b & & & b \\ \vdots & & \ddots & & \vdots \\ b & & \cdots & a+b & b \\ b & b & & b & a+b \end{bmatrix}_{6\times 6}. \tag{10}$$

Given a global XY Cartesian coordinate system, the kinematic stretch-strain relationship, assuming homogeneous small strain deformations, is derived as

$$S_{ij} = \left(N_{xij}\right)^2 \varepsilon_x + \left(N_{yij}\right)^2 \varepsilon_y + N_{xij} N_{yij} \gamma_{xy}, \tag{11}$$

and in matrix form as

$$\boldsymbol{S}_i = \boldsymbol{N}_i \boldsymbol{\varepsilon}_i, \tag{12}$$

where the stretch vector is $\boldsymbol{S}_i = \left[S_{ij}\right]_{6\times 1} = \left\{S_{i1}, \dots, S_{ij}, \dots, S_{i6}\right\}$, the strain vector is $\boldsymbol{\varepsilon}_i = \left\{\varepsilon_x, \varepsilon_y, \gamma_{xy}\right\}_i$, and the transformation matrix, $\boldsymbol{N}_i$, is defined as

$$\boldsymbol{N}_i = \begin{bmatrix} (N_{xi1})^2 & \left(N_{yi1}\right)^2 & N_{xi1} N_{yi1} \\ \vdots & \vdots & \vdots \\ \left(N_{xij}\right)^2 & \left(N_{yij}\right)^2 & N_{xij} N_{yij} \\ \vdots & \vdots & \vdots \\ (N_{xi6})^2 & \left(N_{yi6}\right)^2 & N_{xi6} N_{yi6} \end{bmatrix}_{6\times 3}. \tag{13}$$

Here, N_{xij} is the direction cosine between bond *ij* and the *x*-axis in the reference configuration, and so on.

To find the peridynamic elastic constants a and b for a finite volume ΔV_i of a linear-elastic solid in terms of the classical elastic moduli *E* and ν associated with particle *i*, the strain energies stored by equivalent volumes of the classical linear-elastic model and the SPLM particle are assumed to be identical under the equivalent deformation states:

$$\delta W_{Classical} = \delta W_{SPLM}; \text{ therefore } \boldsymbol{\sigma}_i{}^T \delta \boldsymbol{\varepsilon}_i \Delta V_i = \frac{1}{2} \boldsymbol{F}_{\boldsymbol{S}_i}^T \boldsymbol{L}_{0_i} \delta \boldsymbol{S}_{\boldsymbol{e}_i}, \tag{14}$$

where $\delta \boldsymbol{S}_{\boldsymbol{e}_i}$ and $\delta \boldsymbol{\varepsilon}_i$ are, respectively, the kinematically equivalent elastic stretch states and strain vectors, $\boldsymbol{\sigma}_i = \left\{\sigma_x, \sigma_y, \tau_{xy}\right\}_i$ is the classical Cauchy stress, and $\boldsymbol{L}_{0_i}$ is the diagonal reference bond length matrix

$$\boldsymbol{L}_{0_i} = \begin{bmatrix} L_0 & 0 & \cdots & & 0 \\ 0 & & & & \\ \vdots & & \ddots & & \vdots \\ & & & & 0 \\ 0 & & \cdots & 0 & L_0 \end{bmatrix}_{6\times 6} = L_0 \boldsymbol{I} \quad \text{(for the 2D case).} \tag{15}$$

By substituting Eq. (12) into Eq. (14) and recognizing that $\delta\boldsymbol{\varepsilon}$ is arbitrary and therefore can be dropped from both sides of the equation, we obtain the relation for the stress at particle i:

$$\boldsymbol{\sigma}_i = \boldsymbol{M}_i \boldsymbol{F}_{\boldsymbol{S}_i}, \tag{16}$$

where $\boldsymbol{M}_i = \frac{1}{2\Delta V_i} \boldsymbol{L}_{0_i} \boldsymbol{N}_i{}^T$. From the classical linear-elastic theory [Sadd (2009)], the stress-strain relation is

$$\boldsymbol{\sigma}_i = \boldsymbol{D}\boldsymbol{\varepsilon}_i, \tag{17}$$

where $\boldsymbol{D}_{3\times 3}$ is the classical plane strain or plane stress elastic stiffness matrix. By substituting Eq. (9) into Eq. (16), and equating Eqs. (16) and (17); the following constitutive relation for particle i is derived

$$\boldsymbol{D} = \boldsymbol{M}_i \boldsymbol{K}_i \boldsymbol{N}_i \ . \tag{18}$$

For particles in the reference configuration and in the bulk material, Eq. (18) represents a system of equations, with 9 equations and 2 unknowns: The SPLM peridynamic elastic moduli a and b. Assuming a linear elastic isotropic material, the peridynamic micro-elastic constants are functions of Young's modulus E and the Poisson's ratio ν.

We ignore the fact that boundary particles have fewer bonds, and assume that $\boldsymbol{K}$ is valid for all the horizons in the domain. Further, we associate the same material volume (ΔV) with all the particles in reference configuration (including boundary particles), and assume an invariant $\boldsymbol{N}$ matrix (Eq. (13)). Finally, we solve Eq. (18) to obtain the peridynamic elastic constants a and b for plane stress as

$$a = \frac{2EL_0 t}{\sqrt{3}(1+\nu)}, \ b = \frac{EL_0 t(1-3\nu)}{6\sqrt{3}(\nu^2-1)}, \tag{19}$$

(note the factor of 2 error for b in Gerstle [Gerstle (2015)]), and for plane strain as

$$a = \frac{2EL_0 t}{\sqrt{3}(1+\nu)}, \ b = \frac{EL_0 t(1-4\nu)}{6\sqrt{3}(2\nu-1)(\nu+1)}, \tag{20}$$

where E is Young's modulus, ν is Poisson's ratio, t is the material thickness, and L_0 is the reference lattice spacing. As can be seen, with the SPLM, the elastic constants a and b are obtained with reference to the lattice, and without the need for solving integral equations over a continuum domain. If the deformations are small, homogeneous, and far from a boundary, the SPLM elastic solution is linear and matches the classical elastic solution. However, the SPLM simulates large gradients of the deformation field in a reasonable manner that is not matched by small-deformation classical linear elasticity theory. Although the elastic bond forces are linearly related to bond stretches, because bond rotations may be large, the presented elastic SPLM forces are not linear with respect to particle positions because the bond stretches are not linearly related to particle positions.

The SPLM exhibits physically plausible boundary effects, which can be refined based upon experimental evidence. This is different from classical elasticity, which (without

modification) does not include boundary effects, even where they might physically exist. As the lattice spacing decreases, the boundary effects have a decreasing effect upon the overall elastically stored energy.

2.2 SPLM plasticity model

In this section, a plasticity model for the SPLM is presented. The yield criterion, flow rule, and model for the evolution of the yield surface, including both plastic hardening and plastic softening, are described. The plasticity model developed here is similar to the classical J_2 plasticity model, with an evolving Von Mises yield surface. In the SPLM, the plasticity model is expressed in terms of bond forces and plastic bond stretches, rather than in terms of stresses and strains. Because the lattice model has a built-in localization limiter (the lattice spacing L_0), plastic softening can be accommodated, unlike with the classical plasticity model, where softening plastic strains become unbounded.

In classical continuum theory, the stress tensor, $\boldsymbol{\sigma}$, is decomposed in terms of deviatoric, $\boldsymbol{\sigma}_d$, and hydrostatic, $\boldsymbol{\sigma}_h$, stresses as $\boldsymbol{\sigma} = \boldsymbol{\sigma}_d + \boldsymbol{\sigma}_h$. The hydrostatic stress $\boldsymbol{\sigma}_h$ is the average of the diagonal components (normal components) of the stress tensor $\boldsymbol{\sigma}_h = \frac{1}{3}\big(tr(\boldsymbol{\sigma})\big)\boldsymbol{I}$; therefore, the deviatoric stress tensor is expressed as

$$\boldsymbol{\sigma}_d = \boldsymbol{\sigma} - \boldsymbol{\sigma}_h = \boldsymbol{\sigma} - \frac{1}{3}(tr(\boldsymbol{\sigma}))\,\boldsymbol{I}. \tag{21}$$

In the SPLM linear-elastic model, the relation between the classical stress vector, $\boldsymbol{\sigma}$, and the force state vector is expressed using Eq. (16) as $\boldsymbol{\sigma} = \boldsymbol{M}\boldsymbol{F}_{\boldsymbol{S}}$, and the stress components of $\boldsymbol{\sigma}$ can therefore be expressed in terms of the force state. Thus, the equivalent deviatoric stress tensor $\boldsymbol{\sigma}_d$ in terms of the force state $\boldsymbol{F}_{\boldsymbol{S}}$ can be computed. Finally, the equivalent J_2 plasticity for SPLM is defined as one-half of the L_2 norm of the equivalent deviatoric stress tensor as

$$J_2 = \frac{1}{2}\|\boldsymbol{\sigma}_d\|_2 . \tag{22}$$

The yield condition is implemented by defining a yield indicator

$$Y = \frac{J_2}{\left(\left(F_{Yeff}\right)^2/3\right)}, \tag{23}$$

where F_{Yeff} is the current uniaxial yield stress. The yield condition is reached when $Y \geq 1$.

The linear plastic hardening (see Fig. 3c) as well as time-dependent plastic softening are modelled via the effective yield function, F_{Yeff}:

$$\begin{cases} {F_{Yeff}}^{n+1} = max\left\{{F_{Yeff}}^{n}\ , f_y + \left(\frac{f_u - f_y}{\varepsilon_{ult}}\right){\varepsilon_{\mathrm{p}}}_{eff}^{\ n}\right\} & if \quad {\varepsilon_{\mathrm{p}}}_{eff}^{\ n} < \varepsilon_{ult} \\ {F_{Yeff}}^{n+1} = \vartheta {F_{Yeff}}^{n} & if \quad {\varepsilon_{\mathrm{p}}}_{eff}^{\ n} \geq \varepsilon_{ult} \end{cases} \tag{24}$$

where f_y and f_u are, respectively, the classical yield strength and ultimate strength of the material, ε_{ult} is the ultimate failure strain, ϑ is a rate-dependent plastic softening parameter (set to 0.99), and the effective plastic strain, ${\varepsilon_{\mathrm{p}}}_{eff}$, is defined as

$$\varepsilon_{p_{eff}} = \sqrt{{\varepsilon_{p_1}}^2 - \varepsilon_{p_1}\varepsilon_{p_2} + {\varepsilon_{p_2}}^2} \quad , \tag{25}$$

where ε_{p_1} and ε_{p_2} are the principal plastic strain components.

To calculate the plastic flow, the incremental plastic stretch $(\Delta S_P)_{ij}$ is computed. This approach was initially introduced by Gerstle [Gerstle (2015)], and an improved version is presented in this study. It is assumed that in analogy to Eq. (21), the plastic flow is proportional to the deviatoric components of the bond force vector, as follows.

$$\boldsymbol{F_{b_{dev}}} = \boldsymbol{F_b} - F_{b_{avg}} \, . \tag{26}$$

Here, $\boldsymbol{F_{b_{dev}}}$ is the deviatoric part of the bond force vector, $\boldsymbol{F_b}$ is the bond force vector (from Eq. (5)), and $F_{b_{avg}}$ is the average of the components of $\boldsymbol{F_b}$, defined as

$$F_{b_{avg}} = avg(\boldsymbol{F_b}) = \frac{1}{6}\sum_{j=1}^{6}(F_b)_{ij}. \tag{27}$$

The incremental plastic stretch vector in the time step, $\Delta \boldsymbol{S_P} = [(\Delta S_P)_{ij}]_{6\times 1}$, is then computed as

$$\Delta \boldsymbol{S_P} = \Delta\lambda \frac{\boldsymbol{F_{b_{dev}}}}{\|\boldsymbol{F_{b_{dev}}}\|_2}, \tag{28}$$

where

$$\Delta\lambda = \ min(\Delta S_{pmax}, \frac{f_y}{E}\ (Y-1)). \tag{29}$$

Here, $\Delta\lambda$ is the SPLM flow parameter, analogous to Levy-Mises flow constant from the classical theory, E is Young's module and f_y is the yield strength of material. $\Delta S_{pmax} = 0.01$ is a maximum permissible plastic stretch increment per time step, necessary to preserve stable plastic deformation behavior during plastic softening. Finally, the plastic stretch of particle bond ij, at time step $n\ +1$, $(S_P)_{ij}^{n+1}$, is computed as

$$(S_P)_{ij}^{n+1} = (S_P)_{ij}^{n} + (\Delta S_P)_{ij}^{n}, \tag{30}$$

and by substituting Eq. (30) into Eq. (7), the elastic stretch of bond ij is calculated. Each particle in the lattice stores its six plastic bond stretches, as well as its current effective yield stress F_{Yeff}, as state variables.

2.3 Two-spring damage model

In this section, a novel "two-spring" damage model that enables damage localization and crack formation is proposed for the SPLM. In this model, an elastic bond is approximated as two equal (undeformed) length serial springs. The damage parameter ω_i, assumed as a scalar, is associated with the lattice particle i instead of with bond ij, as has typically been assumed in continuum peridynamics. In this isotropic, particle-based scalar damage model, the damage parameter ω_i evolves as a function of the force state and the stretch state. Because the damage in two adjacent particles may be quite different, this model allows for differential stretches in the two half-bonds connecting the particles, as shown in Fig. 2. Thus, the stretch states of two neighboring particles, and hence their damage

paramters, may be very different. If either particle i or particle j is fully damaged, the bond force is null.

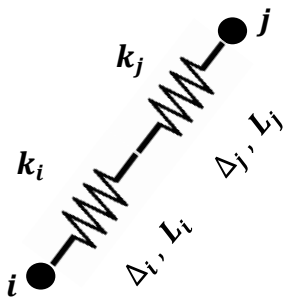

Figure 2: Representation of a peridynamic bond by two serial springs

Fig. 2 shows two serial springs of undeformed length $L_i = {}^{L_0}/_2$ and $L_j = {}^{L_0}/_2$ representing a bond of undeformed length L_0. The force-displacement relations of the two springs are defined by $F_i = k_i\Delta_i = k_i S_i L_i$ and $F_j = k_j\Delta_j = k_j S_j L_j$. Force equilibrium of the two springs mandates that $F_i = F_j$ and the kinematics of the spring system requires that $\Delta = \Delta_i + \Delta_j$. Using these equations, the ratio of displacements of two serial springs is obtained as

$$\frac{\Delta_j}{\Delta_i} = \frac{k_i}{k_j}. \tag{31}$$

Also, the equivalent stiffness of the serial springs system, k_{eq}, is derived as

$$\frac{1}{k_{eq}} = \frac{1}{k_i} + \frac{1}{k_j} \quad \text{and} \quad k_{eq} = \frac{k_i k_j}{k_i + k_j}, \tag{32}$$

and the relationship between the stretch of each half-bond and the overall bond stretch S_{ij} is obtained as

$$S_i = \left(\frac{2k_j}{k_i + k_j}\right) S_{ij} \qquad \text{and} \qquad S_j = \left(\frac{2k_i}{k_i + k_j}\right) S_{ij}. \tag{33}$$

We assume that the stiffness of each half spring is related to the damage in the associated particle:

$$k_i = (1 - \omega_i)\frac{a_i}{\left({}^{L_0}/_2\right)} \text{ and } k_j = \left(1 - \omega_j\right)\frac{a_j}{\left({}^{L_0}/_2\right)} \tag{34}$$

Assuming that $a_i = a_j = a$, we define the *modified* stretch state S_{ij}^* at particle i as

$$S_{ij}^* = \left(\frac{2k_j}{k_i + k_j}\right) S_{ij} = \left(\frac{2(1-\omega_j)\left(\frac{2a}{L_0}\right)}{(1-\omega_i)\left(\frac{2a}{L_0}\right) + (1-\omega_j)\left(\frac{2a}{L_0}\right)}\right) S_{ij} = \left(\frac{2(1-\omega_j)}{2 - \omega_i - \omega_j}\right) S_{ij}. \tag{35}$$

The modified elastic stretch state of particles i and j, $(S_e^*)_{ij}$ and $(S_e^*)_{ji}$, accounts for differing stiffnesses of damaged particles *i* and *j*. For boundary particles having bonds *j* with no neighbors, the damage ω_j is assumed to be unity. If both $\omega_i = 1$ and $\omega_j = 1$, then we assume that the modified bond stretch $S_{ij}^* = S_{ij}$. Note that if particle i is

undamaged and particle *j* is fully damaged, then $S_{ij}^{*} = 0$, and that if particle *i* is fully damaged and particle *j* is undamaged, then $S_{ij}^{*} = 2S_{ij}$.

We now express the force state at particle i in terms of the *modified elastic* stretch state as

$$(F_s)_{ij} = (1-\omega_i)\left[a\left(S_e\right)_{ij}^{*} + b\sum_{m=1}^{6}\left(S_e\right)_{im}^{*}\right]. \tag{36}$$

In the case of no damage, Eq. (36) simplifies to Eq. (6).

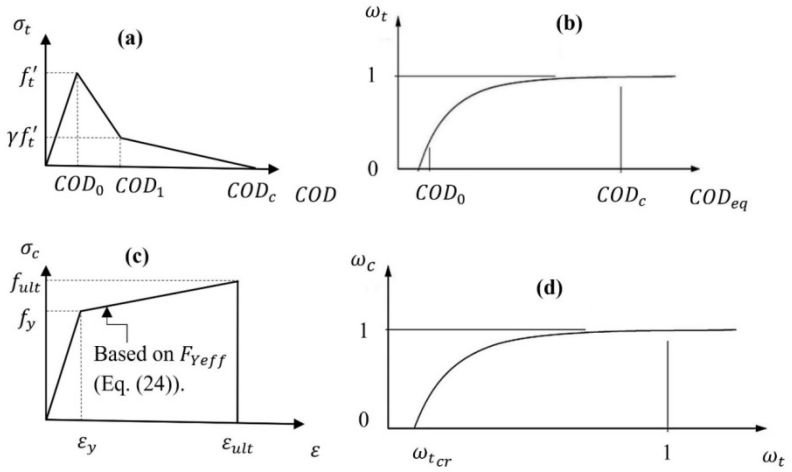

Figure 3: Mechanical behavior of concrete defined in SPLM and the definition of the damage parameters. (a) Bilinear uniaxial tensile strength-COD (tension softening) relation. (b) Tensile damage parameter, ω_t-COD_{eq} relation. (c) Compressive stress verus strain relation with linear hardening. (d) Compressive damage parameter, ω_c , versus ω_t

Tensile damage ω_i initiates at particle i when the maximum positive principal stress component exceeds the tensile strength f_t' and the minimum of the other principal stress components exceeds $-\varrho f_t'$. The parameter ϱ is called the tension-compression parameter which incorporates the multiaxial state of stress into the damage initiation criterion in a simple way (without need for defining a more complicated failure surface). The tensile damage parameter, ω_i, evolves in a manner similar to the Hillerborg fictitious crack model [Hillerborg, Modéer and Petersson (1976)]. The evolution of tensile damage (tension softening) of concrete is simulated via the bilinear tensile strength-*COD* curve shown in Fig. 3a.

By calculating the principal strain components associated with particle *i* (ε_1^{*} and ε_2^{*}) based upon the modified stretch state $(S_e^{*})_{ij}$ (using Eq. (12)), the equivalent crack opening displacement (COD_{eq}) associated with particle *i* is calculated as

$$\left(COD_{eq}\right) = L_0\varepsilon_{\text{crack}}^{*}, \tag{37}$$

where $\varepsilon_{\text{crack}}^{*}$ is the elastic crack band strain defined as

$$\varepsilon_{\text{crack}}^{*} = \sqrt{\varepsilon_1^{*2} - \varepsilon_1^{*}\varepsilon_2^{*} + \varepsilon_2^{*2}}. \tag{38}$$

Note that with this definition of the equivalent crack opening displacement (COD_{eq}), once damage ω_i has initiated at a particle, the damage can grow even under compressive strain conditions. This allows damage, once initiated, to evolve in both tensile and compressive regimes as are found in multiaxial problems such as the Brazilian split cylinder test. To avoid unrealistic damage and plasticity initiation from the boundaries due to artificially high stresses computed on the boundary particles; we introduce a boundary parameter, β_1, with which the artificially high stress computed at boundary particles is reduced. Setting β_1 less than unity retards crack initiation at boundaries.

Depending on whether the bond is under tension or compression, the damage parameter ω_i evolves as follows: If $(S_e)_{ij} \geq 0$, then $\omega_i = (\omega_t)_i$ and

$$(\omega_t)_i = \begin{cases} 0 & if \quad COD_{eq} < 0 \\ 1 - \left(\frac{f_t'}{ECOD_1 \varepsilon^*_{\text{crack}}}\right)\left(COD_1 + (\gamma - 1)COD_{eq}\right) & if \quad 0 \leq COD_{eq} < COD_1 \\ 1 & if \quad COD_{eq} \geq COD_c \end{cases}, \tag{39}$$

else if $(S_e)_{ij} < 0$, then $\omega_i = (\omega_c)_i$ and

$$(\omega_c)_i = \begin{cases} \frac{\sqrt{(\omega)_i} - \sqrt{(\omega_{t_{cr}})_i}}{1 - \sqrt{(\omega_{t_{cr}})_i}} & if \quad (\omega_t)_i > (\omega_{t_{cr}})_i \\ 0 & if \quad (\omega_t)_i \leq (\omega_{t_{cr}})_i \end{cases} \tag{40}$$

Here, $(\omega_t)_i$ and $(\omega_c)_i$ are, respectively, the tensile and compressive damage parameters associated with particle *i*, *E* is the Young's modulus, f_t' is the tensile strength, $\gamma f_t'$ is the tensile damage constant at the "knee", COD_c is the critical crack opening displacement, and COD_1 is the crack opening displacement at the "knee", as shown in Figs. 3a and 3b. The tensile damage parameter, ω_t, varies in a nonlinear fashion and grows to unity as the equivalent crack opening displacement COD_{eq} increases. When COD_{eq} reaches COD_0, the damage parameter immediately jumps to a finite value, rather than gradually increasing from zero (as shown in Fig. 3b). In Eq. (40), $\omega_{t_{cr}}$ is the critical tensile damage parameter which is assumed as the threshold for initiating partial compressive damage. Note that the damage behavior due to cyclic loading steps is not studied in this paper. However, changing the state of particles as they go from tension to compression regimes (and vice versa) is recognized and modelled using the compression damage parameter ω_c.

As can be seen from the proposed formulation, elasticity, plasticity and damage are coupled in this model.

2.4 Numerical implementation of SPLM

In this section, the numerical implementation of the improved SPLM method is briefly discussed and the important issues regarding the new algorithm are expressed and elaborated.

The form of a particle family in the re-formulated SPLM approach is shown in Fig. 1b. Considering Fig. 1b, the SPLM equation of motion, defined in Eq. (3), can be re-written (including damping) as

$$\ddot{\boldsymbol{X}}_i^n = \frac{1}{m_i}\left[\sum_{j=1}^{6}\left\{(\boldsymbol{F_b})_{ij}^n + d_{ij}^n\left(\boldsymbol{F_{dampint}}\right)_{ij}^n\right\} + \left(\boldsymbol{F_{dampext}}\right)_i^n + \boldsymbol{B}_i^n\right], \tag{41}$$

where both internal and external damping forces, $\boldsymbol{F_{dampint}}$ and $\boldsymbol{F_{dampext}}$, are now included. In the new SPLM, the damping force depends upon the damage. Calculation of damping forces is similar as in the initial SPLM (more details can be found in Gerstle [Gerstle (2015)]). However, to improve the simulation of dynamic effects on the post-peak region, the internal damping force $\boldsymbol{F_{dampint}}$ is multiplied by a factor, d_{ij}. The factor d_{ij} is defined, based upon Eqs. (32) and (34), as $d_{ij} = 2(1-\omega_i)(1-\omega_j)/(2-\omega_i-\omega_j)$. As damage increases, the damping coefficient decreases. Thus, when either of the particles connected by a bond becomes fully damaged, the damping force is reduced to zero.

After calculating $\ddot{\boldsymbol{X}}_i^n$ from Eq. (41), the velocity of particle i, $\dot{\boldsymbol{X}}_i^{n+1}$, is calculated using a first order forward difference as

$$\dot{\boldsymbol{X}}_i^{n+1} = \dot{\boldsymbol{X}}_i^n + \Delta t\ddot{\boldsymbol{X}}_i^n\,, \tag{42}$$

and the position of particle i, $\boldsymbol{X}_i^{n+1}$, is calculated using a first order backward difference, as

$$\boldsymbol{X}_i^{n+1} = \boldsymbol{X}_i^n + \Delta t\dot{\boldsymbol{X}}_i^{n+1}. \tag{43}$$

where Δt is the time step (the critical time step, Δt_{crit}, is derived in Gerstle [Gerstle (2015)]). One of the main differences between the new SPLM formulation and the initial version is the method for storing particle attributes. In the re-formulated SPLM algorithm, the values of the bond forces, damage parameters, and plastic stretches are calculated and stored in the two consecutive time steps n-1 and n. This ensures that the computed particle responses are independent of the order in which the particles are visited within a given time step.

3 Example simulations

In this section, three plain concrete benchmark problems are simulated: The uniaxial tension specimen, the uniaxial compression specimen, and the Brazilian split cylinder, shown in Fig. 4.

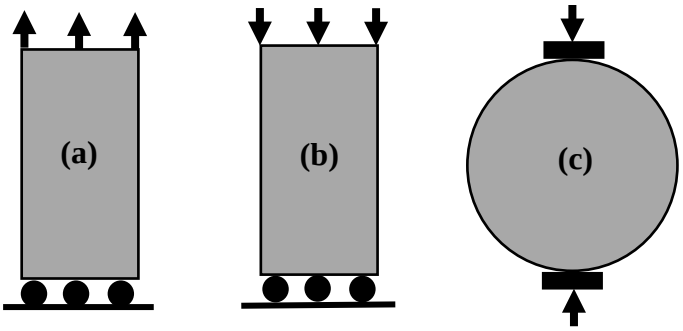

Figure 4: Schematic of the problem domains and boundary conditions of the considered concrete specimens. (a) Uniaxial tension, (b) Uniaxial compression, (c) Brazilian split cylinder

Each problem is simulated with the re-formulated plain-stress SPLM approach described in this paper (SPLM-2018) and compared with the results of the previous version [Gerstle (2015)] (SPLM-2016). To investigate the objectivity of the method, each problem is simulated using three different lattice rotations. The results are compared, as far as possible, to classical elasticity/plasticity/fracture mechanics methods. Typical material properties for normal-strength concrete are used [ACI Committee 318 (2014)]. The simulation parameters are shown in Tab. 1. All the simulations in this study were conducted on a single-core laptop and each simulation finished in less than three minutes.

Table 1: Classical and SPLM parameters used for example problems

Parameter	Symbol	Value	Units
Young's modulus, shown in Fig. 3c	E	25	*GPa*
Mass density	$\boldsymbol{\rho}$	2323	Kg/m^3
Poisson's ratio	$\boldsymbol{\nu}$	0.2	-
Critical tensile damage parameter, shown in Fig. 3a	$\boldsymbol{\omega_{t_{cr}}}$	0.8	-
Plastic strain at which complete damage occurs, shown in Fig. 3c	$\boldsymbol{\varepsilon_{plast(ult)}}$	0.003	-
Internal material damping ratio	$\boldsymbol{\xi_{internal}}$	0.2	-
External damping ratio	$\boldsymbol{\xi_{external}}$	0.2	-
Yield strength, shown in Fig. 3c	$\boldsymbol{f_y}$	22.98	*MPa*
Ultimate strength, shown in Fig. 3c	$\boldsymbol{f_u}$	27.58	*MPa*
Tension-compression parameter	$\boldsymbol{\varrho}$	6.0	-
Boundary parameter	$\boldsymbol{\beta_1}$	0.2	-
Tensile strength causing damage initiation, shown in Fig. 3a	$\boldsymbol{f_t}$	2.62	*MPa*
Crack opening displacement at knee of curve, shown in Fig. 3a	$\boldsymbol{COD_1}$	$2x10^{-5}$	*m*
Critical crack opening displacement, shown in Fig. 3a	$\boldsymbol{COD_c}$	$2x10^{-4}$	*m*
Ratio of stress at "knee" to $\boldsymbol{f_t}$, shown in Fig. 3a	$\boldsymbol{\gamma}$	0.25	-

3.1 Uniaxial tension and compression specimens

A rectangular concrete specimen 0.3 *m* high by 0.15 *m* wide by 0.15 *m* thick is subject to uniaxial loading. The lattice spacing is $L_0 = 0.01\ m$. The boundary conditions are defined such that the bottom boundary is fixed in the vertical direction only, and a smoothly time-varying displacement

$$\Delta_y(t) = \left(\frac{\Delta_{max}}{2}\right)\left(1 - \cos\left(\frac{\pi t}{t_{ramp(end)}}\right)\right) \tag{44}$$

is applied to the top boundary, as shown in Fig. 4a. The displacement boundary conditions are applied to all lattice particles within L_0 of top and within L_0 of the bottom of the specimen (shown in the Fig. 5 by green particles).

In Eq. (44), Δ_{max} is the maximum applied displacement assumed to be calculated as $\Delta_{max} = 1.5COD_c$ for the tension problem and $\Delta_{max} = -6COD_c$ for the compression problem; $t_{ramp(end)} = 0.8t_{end}$, and t_{end} is calculated based on the fundamental period of vibration of the specimen and the time stepping increment (more details can be found in [Gerstle (2015)]). The fundamental period of the each specimen is calculated from a linear elastic modal analysis. For these problems, a fundamental period of 0.00035 *s* is estimated. The time step is $\Delta t_{\text{crit}} = 6.55 \times 10^{-7}\ s$ is used and the simulations employ 77000 time steps. The uniaxial tension and compression problems are simulated with both the SPLM-2016 and the SPLM-2018 methods; each with varying lattice rotations of 0^o, 15^o, and 30^o, including for each lattice rotation 605, 595, and 569 particles, respectively. The cracking patterns obtained for each lattice rotation are shown in Figs. 5 and 6, and the calculated force-displacement curves are shown in Figs. 7 and 8. In Figs. 5 and 6, in addition to damage, the effective plastic strains (Eq. (25)) are displayed. The particles having $\varepsilon_{\text{p}_{eff}} > \varepsilon_{ult}$ are fully black, and the non-black particles have not yielded.

The results show significant improvements (specifically in post-peak region) in SPLM-2018; as well as a better match with the expected classical solutions. In the compression problem, shear bands due to softening plasticity are evident in the simulation results (see gray scale colored particles in Fig. 6). Each simulation required less than three minutes using a single-core laptop computer.

3.2 Brazilian split cylinder

In this problem, a circular cylinder of diameter 0.15 *m* and thickness 0.15 *m*, subjected to external compression forces across its diameter, is simulated. The lattice spacing is $L_0 = 0.005\ m$. The boundary conditions are shown in Fig. 4c. The same time varying displacement (Eq. (44)) is applied at top and bottom of the Brazilian split cylinder models. The specified displacement boundary conditions are applied to the particles at the top and bottom of the specimen (the green particles shown in Fig. 10), to emulate the loading plates. This problem is also solved with both SPLM-2016 and SPLM-2018; each with three different lattice rotations of 0^o, 15^o, and 30^o, with 839, 841, and 843 particles, respectively, for each lattice rotation. The fundamental period is calculated as 0.0002321 *s*. The time step is $\Delta t_{\text{crit}} = 3.27 \times 10^{-7} s$, and the simulations employ 113500 timesteps. The calculated force-displacement curves are shown in Fig. 9, and the damage and plasticity fields obtained for each lattice rotation are shown in Fig. 10. The plastically yielded particles are

shown in black. These results demonstrate the superiority and robustness of the re-formulated SPLM method with respect to SPLM-2016. In addition, a lattice refinement study is performed for the zero-rotation models with a lattice spacing of 0.01 *m*, 0.005 *m*, and 0.0025 *m* including a total number of 213, 839, and 3315 particles, respectively. The obtained cracking patterns are shown in Fig. 11 and the force-displacement relations are shown in Fig. 12.

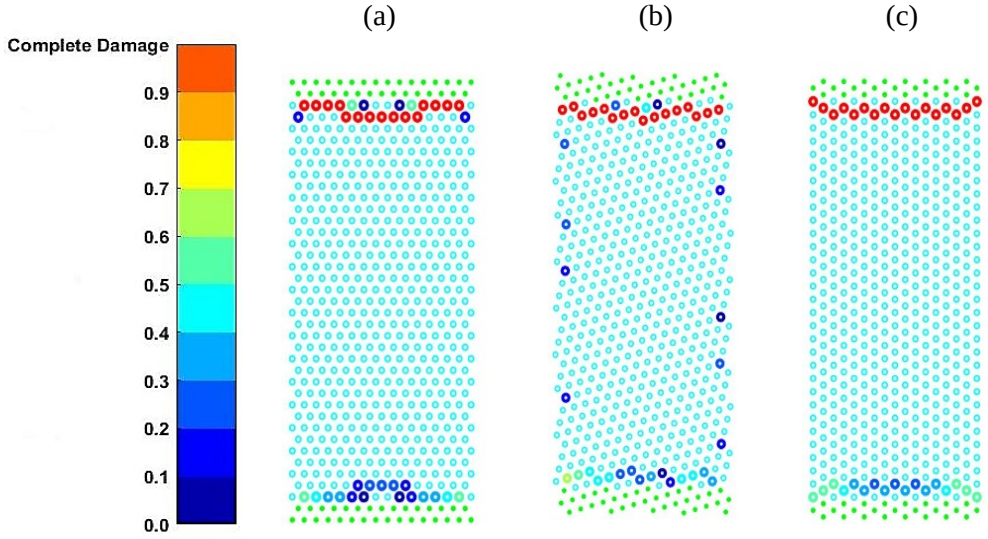

Figure 5: Cracking patterns for uniaxial tension problem at the final time step, for SPLM-2018, with lattice rotations of: (a) 0^o, (b) 15^o, and (c) 30^o

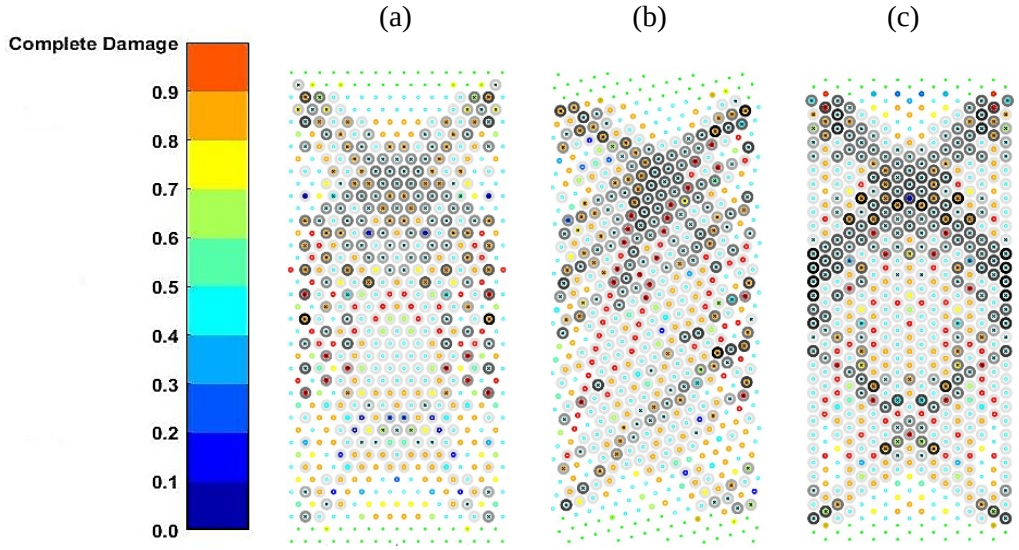

Figure 6: Cracking patterns for uniaxial compression problem at the final time step, for SPLM-2018, with lattice rotations of: (a) 0^o, (b) 15^o, and (c) 30^o (Gray scale color shows the effective plastic strain)

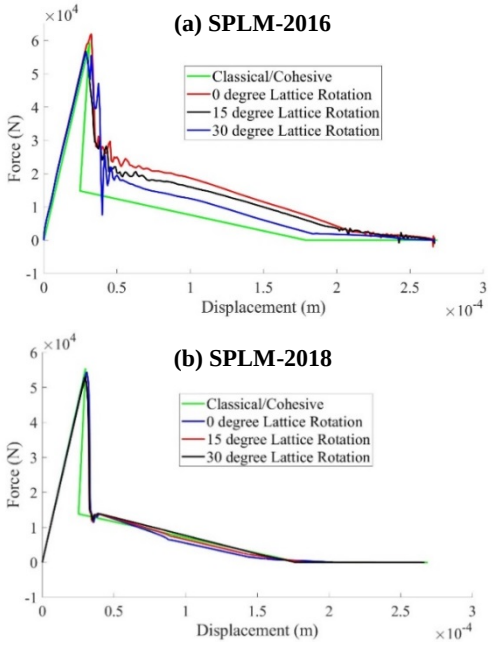

Figure 7: Comparison between SPLM-2016 and SPLM-2018 for uniaxial tension problem

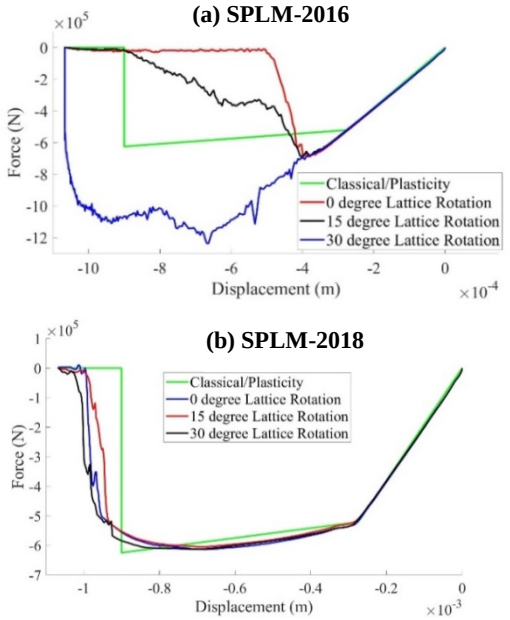

Figure 8: Comparison between SPLM-2016 and SPLM-2018 for uniaxial compression problem

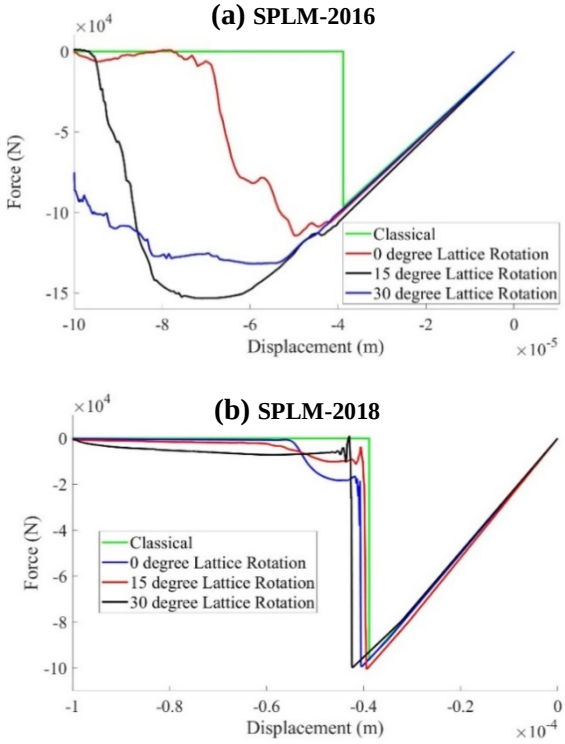

Figure 9: Comparison between SPLM-2016 and SPLM-2018 for Brazilian split cylinder problem

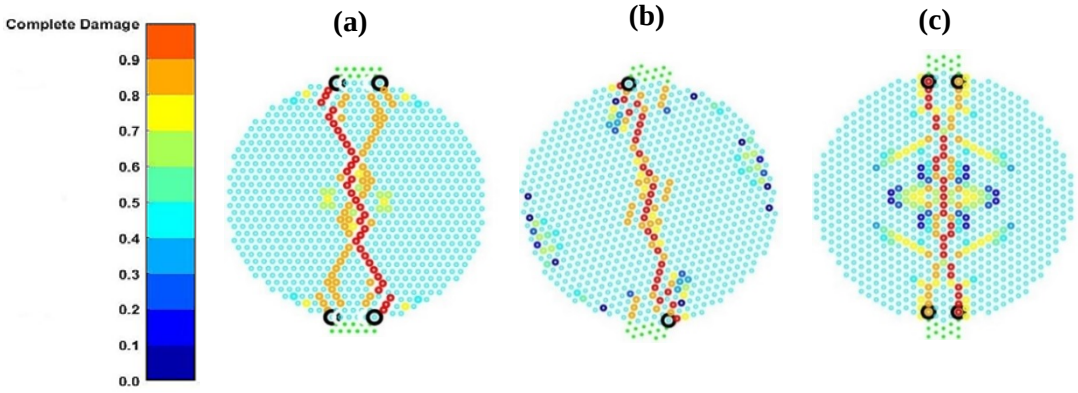

Figure 10: Simulated cracking patterns for Brazilian split cylinder problem at the final timestep, for SPLM-2018, with lattice rotations of: (a) 0^o, (b) 15^o, and (c) 30^o

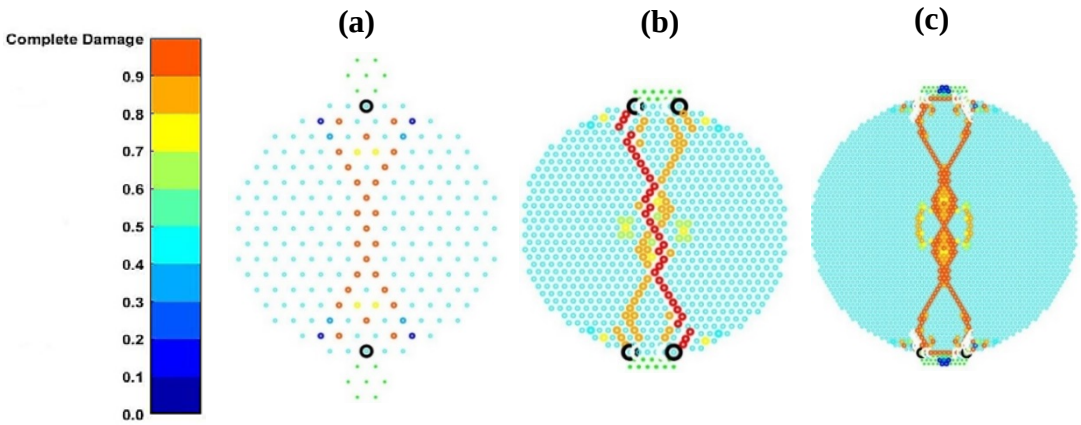

Figure 11: Simulated cracking patterns for Brazilian split cylinder problem at the final timestep, for SPLM-2018, with: (a) $L_0 = 0.01\ m$, $N_{steps} = 56800$ (b) $L_0 = 0.005\ m$, $N_{steps} = 113500$ and (c) $L_0 = 0.0025\ m$, $N_{steps} = 226900$

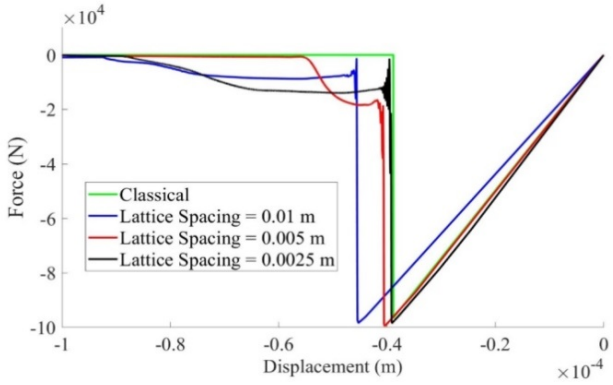

Figure 12: Lattice refinement study (SPLM-2018) for Brazilian split cylinder problem (Lattice rotation angle of 0°)

3.3 Comparison with the experimental data

The efficiency and practicality of SPLM in modelling concrete is demonstrated by reviewing the literature related to the mechanical properties of concrete and comparing it with the simulation results from the SPLM.

The statistical variation in compressive strength of apparently identical normal-strength concrete samples is shown in Fig. 13 [Wight (2016)]. As can be seen, for the uniaxial compressive strength tests of 176 nominally identical samples, there is a distribution of tested strengths. The mean strength is 27.17 MPa (almost the same as f_u =27.58 MPa employed in our SPLM examples), and the coefficient of variation is 15%; which represents *average control* based on the ACI Committee 214 standard [Aci Committee 214 (1956)]. To compare the SPLM simulation results with laboratory results, 31 uniaxial compression simulations are performed, with lattice rotation angles varying from 0^{o} to

30^o with an increment of 1^o, and the normal distribution of the results are plotted in Fig. 13. The coefficient of variation from the SPLM simulations is 1.74% and the mean compressive strength is 28.27 MPa. Comparing distribution of results from SPLM with the distribution in standard tests, the SPLM demonstrates a more than sufficient level of objectivity in predicting the compressive strength of concrete.

Large discrepancies in the splitting tensile strength of concrete are also apparent as shown in Fig. 14, where, as can be seen, for a compressive strength of 27.58 MPa (for ordinary concrete), the splitting tensile strength varies approximately from 1.4 MPa to 3.5 MPa. The classical equation for calculating the peak load of the Brazilian split cylinder test based on the splitting tensile strength is $P_{max} = (\pi l r f'_{ct})/(1-\beta^2)^{1.5}$, where l is the specimen length, r is the radius, $\beta = (w_b/2r)$, w_b is the width of the loading block (here, $w_b = r/3$), f'_{ct} is the splitting tensile strength, and P_{max} is the peak load [Rocco, Guinea, Planas et al. (2001)]. Based on our input data, the experimental peak load falls in the range from 50 KN to 130 KN. P_{max} obtained from the SPLM results is approximately 98 KN (Figs. 9 and 12), falling squarely within the range of the laboratory results. In addition, Fig. 14 shows the range of the splitting tensile strengths of the 31 SPLM simulations. Clearly, the SPLM simulation results more than satisfy the level of objectivity needed. To emphasize the computational efficiency of the SPLM method, note that all the mentioned 31 simulations were computed in less than ten minutes on a single-core laptop machine.

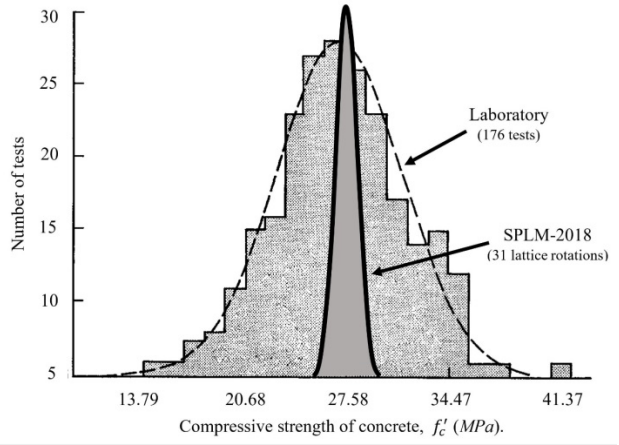

Figure 13: Distribution of compressive strengths of ordinary concrete (after [Wight (2016)])

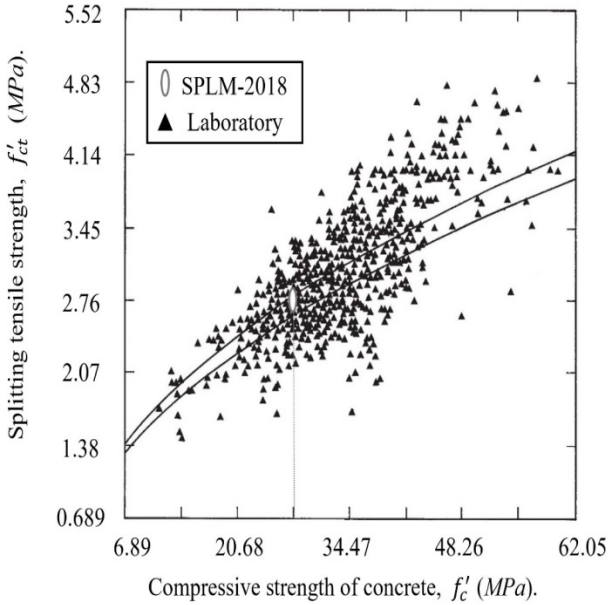

Figure 14: Relationship between splitting tensile strengths and compression strengths (after [Wight (2016)])

Varying crack propagation patterns are common in concrete experimental tests. Fig. 15 shows the cracking results from Brazilian split cylinder tests performed at the University of New Mexico and other available cracking patterns from the literature [Chen, Ge, Zhou et al. (2017)]. The experimental results illustrate the tortuosity and randomness of the cracking. Comparing Fig. 15 with Fig. 10, the SPLM predicts sufficiently objective and realistic cracking and damage patterns.

Figure 15: Crack propagation patterns observed in the Brazilian split cylinder test

4 Conclusions

In this study, the formulation of an improved state-based peridynamic lattice model (SPLM) has been presented. We introduced a novel "two-spring damage model" and an improved hardening-softening-damage plasticity model within the SPLM framework. We

used the reformulated SPLM to simulate three common concrete laboratory tests using varying lattice rotations and lattice spacings. We then compared the SPLM simulation results with those of classical solutions and laboratory results. The outcomes of this study are summarized as follows.

(1) The SPLM is an engineering simplification of continuum state-based peridynamics, based upon a lattice of discrete particles (or alternately, an extension of the conventional theory of lumped-mass spring systems, incorporating state-based peridynamics concepts). The advantages of the SPLM method are listed as follows. (a) Unlike continuum peridynamics and other continuum-based methods, the assumption of continuity of the problem domain is unnecessary. (b) The SPLM is more computationally efficient than continuum peridynamics, requiring fewer particles in each particle's family than continuum peridynamic methods; (c) The SPLM formulation is relatively simple. Implementation of damage and plasticity models is convenient and computationally efficient within the SPLM framework.

(2) With the SPLM some objectivity is sacrificed. Although SPLM increases the computational efficiency of the approach, it is not entirely objective. The lattice model, with lattice spacing of approximately the aggregate size, is sufficient for modeling the geometry and behavior of concrete structures.

(3) While not objective in the continuum sense, the SPLM produces simulation results that are sufficiently objective to be useful in predicting the observed behaviors of concrete tests in the laboratory. As shown in Figs. 13 and 14, a perfectly objective mathematical model would be no more useful than the SPLM in predicting the physical behavior of concrete specimens, which is manifestly random.

(4) A robust coupled elastic-plastic-damage model is successfully implemented for SPLM. Despite the robustness of the approach, some of the presented models are crude and in the first stage of implementation; and can be refined in the future work.

(5) In the re-formulated SPLM algorithm, calculating and storing the bond forces, damage parameters, and plastic stretches are accomplished in two consecutive time steps. This guarantees that the computed particle responses are independent of the order in which the particles are visited within a given time step. One may call this algorithm a "lazy time integration algorithm" which seems to be necessary to obtain algorithmically objective results.

(6) The two-spring damage model (proposed for the SPLM framework) is a novel idea in peridynamic modeling. This model allows highly localized damage to emerge and form cracks as narrow as one lattice particle in width.

(7) The new version of SPLM is more accurate, more objective, and in general more reliable than the previous model in Gerstle [Gerstle (2015)]. The simulation results demonstrate that the new SPLM is capable of simulating many essential behaviors of concrete and produces results similar to laboratory test results.

(8) The changing state of particles as they go from compression to tension regimes (and vice versa), after evolution of damage and plasticity, is recognized and improved in this study; such behaviors are complex and important physical phenomena.

(9) Despite demonstrating similar pre-peak and post-peak behaviors for different lattice rotations and lattice spacings, the SPLM produced somewhat variable, yet plausible, cracking patterns. Such variability is also observed in laboratory tests.

This paper has demonstrated that the SPLM is potentially a useful tool for simulating the behavior of concrete structures under mechanical loading.

Acknowledgements: The authors gratefully acknowledge the University of New Mexico's structural lab and the work of the graduate students Anima Bista and Hari K. Dhamala for providing the photos shown in Fig. 15.

References

ACI Committee 214 (1956): *Evaluation of Compression Test Results of Field Concrete*. National Ready Mixed Concrete Association, Farmington Hills, United States.

ACI Committee 318 (2014): *Building Code Requirements for Structural Concrete (ACI 318-14) and Commentary*. National Ready Mixed Concrete Association, Farmington Hills, United States.

Chen, X.; Ge, L.; Zhou, J.; Wu, S. (2017): Dynamic Brazilian test of concrete using split Hopkinson pressure bar. *Materials and Structures*, vol. 50, no. 1, pp. 1.

Foster, J. T.; Xu, X. (2018): A generalized, ordinary, finite deformation constitutive correspondence model for peridynamics. *International Journal of Solids and Structures*, vol. 141, pp. 245-253.

Gerstle, W.; Sau, N.; Silling, S. (2007): Peridynamic modeling of concrete structures. *Nuclear Engineering and Design*, vol. 237, no. 12, pp. 1250-1258.

Gerstle, W. H. (2015): *Introduction To Practical Peridynamics: Computational Solid Mechanics Without Stress and Strain*. World Scientific Publishing Co Inc., Singapore.

Hattori, G.; Trevelyan, J.; Coombs, W. M. (2018): A non-ordinary state-based peridynamics framework for anisotropic materials. *Computer Methods in Applied Mechanics and Engineering*, vol. 339, pp. 416-442.

Hillerborg, A.; Modeer, M.; Petersson, P. E. (1976): Analysis of crack formation and crack growth in concrete by means of fracture mechanics and finite elements. *Cement and Concrete Research*, vol. 6, no. 6, pp. 773-781.

Macek, R. W.; Silling, S. A. (2007): Peridynamics via finite element analysis. *Finite Elements in Analysis and Design***,** vol. 43, no. 15, pp. 1169-1178.

Mitchell, J.; Silling, S.; Littlewood, D. (2015): A position-aware linear solid constitutive model for peridynamics. *Journal of Mechanics of Materials and Structures*, vol. 10, no. 5, pp. 539-557.

Pasetto, M.; Leng, Y.; Chen, J.; Foster, J. T.; Seleson, P. (2018): A reproducing kernel enhanced approach for peridynamic solutions. *Computer Methods in Applied Mechanics and Engineering*, vol. 340, pp. 1044-1078.

Rabczuk, T.; Ren, H. (2017): A peridynamics formulation for quasi-static fracture and contact in rock. *Engineering Geology*, vol. 225, pp. 42-48.

Rocco, C.; Guinea, G.; Planas, J.; Elices, M. (2001): Review of the splitting-test standards from a fracture mechanics point of view. *Cement and Concrete Research*, vol. 31, no. 1, pp. 73-82.

Sadd, M. H. (2009): *Elasticity: Theory, Applications, and Numerics.* Academic Press, USA.

Seleson, P.; Littlewood, D. J. (2016): Convergence studies in meshfree peridynamic simulations. *Computers & Mathematics with Applications*, vol. 71, no. 11, pp. 2432-2448.

Silling, S. (2017): Stability of peridynamic correspondence material models and their particle discretizations. *Computer Methods in Applied Mechanics and Engineering*, vol. 322, pp. 42-57.

Silling, S.; Lehoucq, R. (2010): Peridynamic theory of solid mechanics. *Advances in Applied Mechanics*, vol. 44, pp. 73-168.

Silling, S.; Littlewood, D.; Seleson, P. (2015): Variable horizon in a peridynamic medium. *Journal of Mechanics of Materials and Structures*, vol. 10, no. 5, pp. 591-612.

Silling, S. A. (2000): Reformulation of elasticity theory for discontinuities and long-range forces. *Journal of the Mechanics and Physics of Solids*, vol. 48, no. 1, pp. 175-209.

Silling, S. A.; Askari, E. (2005): A meshfree method based on the peridynamic model of solid mechanics. *Computers & Structures*, vol. 83, no. 17, pp. 1526-1535.

Silling, S. A.; Epton, M.; Weckner, O.; Xu, J.; Askari, E. (2007): Peridynamic states and constitutive modeling. *Journal of Elasticity*, vol. 88, no. 2, pp. 151-184.

Silling, S. A.; Parks, M. L.; Kamm, J. R.; Weckner, O.; Rassaian, M. (2017): Modeling shockwaves and impact phenomena with Eulerian peridynamics. *International Journal of Impact Engineering*, vol. 107, pp. 47-57.

Wight, J. K. (2016): *Reinforced Concrete: Mechanics and Design, 7th Edition*. Pearson Education, Inc., Hoboken, NJ.

Zadeh, L. A. (1973): Outline of a new approach to the analysis of complex systems and decision processes. *IEEE Transactions on Systems, Man and Cybernetics*, vol. 3, no. 1, pp. 28-44.